

Wind-induced sediment dynamics impact on turbidity for waterworks in Taihu Basin (China) based on numerical simulation

Xinyu Yao (✉ yaoxinyu@zju.edu.cn)

Zhejiang University

Xiaowei Liu

Zhejiang University

Yongchao Zhou

Zhejiang University

Liang Zhang

Huzhou Water Group Co. Ltd

Zhixu Zhou

Huzhou Meteorological Bureau

Yiping Zhang

Zhejiang University <https://orcid.org/0000-0001-8537-8181>

Research Article

Keywords: suspended sediment concentration, waterworks, turbidity, numerical simulation, wind condition, lag effect

Posted Date: April 12th, 2022

DOI: <https://doi.org/10.21203/rs.3.rs-1507446/v1>

License: © ⓘ This work is licensed under a Creative Commons Attribution 4.0 International License.

[Read Full License](#)

1 **Wind-induced sediment dynamics impact on turbidity for**
2 **watrerworks in Taihu Basin (China) based on numerical**
3 **simulation**

4
5 **Xinyu Yao¹, Xiaowei Liu¹, Yongchao Zhou¹, Liang Zhang², Zhixu Zhou³, Yiping Zhang^{1,*}**

6 1. Zhejiang Key Laboratory of Drinking Water Safety and Distribution Technology, Zhejiang
7 University, Hangzhou 310058, China

8 2. Huzhou Water Group Co., Ltd, Huzhou 313000, China

9 3. Huzhou Meteorological Bureau, Huzhou 313005, China

10
11 *Correspondence: Yiping Zhang

12 866# Yuhangtang Road, Hangzhou, Zhejiang, P. R. China

13 Phone: +86-571-88206758

14 Fax: +86-571-88206758

15 Email address: zhangyiping@zju.edu.cn

26 **Abstract:** Lake Taihu is an important drinking water source for cities in the Yangtze River Delta
27 region, while the dramatic fluctuation in turbidity has caused serve problems for local waterworks
28 management. Because the sediment behavior induced by wind disturbance was believed to be the
29 main factor for the matter, the effect of wind fields on the hydrodynamics and sediment distribution
30 of Lake Taihu and the turbidity of the raw water were conducted based on a wind-driven numerical
31 model. The obtained results indicate that wind direction was more influential on the structure of flow
32 and wave fields, while wind speed contributed more to the field intensity, and the suspended sediment
33 of the water intake area primarily consisted of migrated particles from other erosion regions. The high
34 consistency between the simulated suspended sediment concentration and the turbidity with a lag
35 effect of 7 h made it possible for turbidity prediction when combined with the weather forecast
36 technique. The model achieved operation adjustment in advance, thus improving the management
37 efficiency of the waterworks.

38 **Key words:** suspended sediment concentration, waterworks, turbidity, numerical simulation, wind
39 condition, lag effect

40
41
42
43
44
45

46 **1 Introduction**

47 Turbidity refers to the degree of obstruction when the light passing through the solution,
48 including the light scattering by suspended matter and the absorption by solute molecules. It is a
49 crucial index to evaluate the quality of drinking water for waterworks and closely related to the
50 content of impurities (Yue, 1995). However, the violent fluctuations cause problems for dosage
51 adjustment and further operational performance, especially for waterworks with large shallow lakes
52 as supplies. Shallow water bodies characterized by open water-sediment interfaces and small depths
53 are more susceptible to wind fields, thus making the sediment behavior induced by wind disturbance
54 become the main attribution of turbidity variation (Kessarkar et al. 2009; Wu et al. 2013;). When the
55 wind blows over the surface, wind energy is quickly absorbed by the water-air interface and
56 transferred to the bottom layer through breaking waves and turbulence. Once the bottom shear stress
57 is sufficiently large, the sediment layer can be loosened (Bohling 2009), and particles would be
58 stimulated into the overlying water body, resulting in a large sediment flux (Tang et al. 2019). To
59 study the effect of wind-induced hydrodynamics on sediment action and achieve the prediction of
60 suspended sediment concentration (SSC), sediment transport model considering wave effect has been
61 used on some well-known shallow water bodies, such as Lake Balaton in Hungary (Luettich et al.
62 1990), Lake Biwa in Japan (Kumagai 1988), Lake Okeechobee in the United States (Jin and Ji 2001),
63 Poyang Lake (Zhang et al. 2015) and Lake Taihu in China (Qin et al. 2004).

64 As a typical shallow lake in China, Lake Taihu was frequently disturbed by wind for the large
65 water-soil contact and the flat underwater terrain. The large-scale resuspension and migration of
66 sediment caused acute fluctuations in turbidity. Many field observations and laboratory experiments

67 have been conducted in Lake Taihu to investigate the contribution of wind-induced currents and
68 waves on sediment behavior. The bottom shear stress generated by wind-induced waves has been
69 certified to be the main dynamic force for sediment behavior in shallow water bodies (Wu et al. 2013;
70 Luo et al. 2004), while the current-induced shear stress caused by inflow/outflow can be ignored for
71 the negligible effect (Qin et al. 2005; Stone 2011). The former contributed more than 70% to local
72 particle resuspension in shallow lakes and this value even reached 95% in Lake Taihu (Sheng and
73 Lick 1979; Li et al. 2016). Many field studies and experiments have been devoted to studying the
74 relationship between wind fields and sediment concentration by defining the incipient motion of
75 sediment action. The incipient wind speed proposed in previous work ranged from 3m/s to 5 m/s (Jalil
76 et al. 2019; Wu et al. 2013; Zheng et al. 2015), the critical shear stress for sediment resuspension was
77 about 0.02-0.15 N/m² (Zheng et al. 2015; Qiu et al. 2013; Signell et al. 1990). Brand et al. (2010)
78 found that a flow velocity of 0.01 m/s was a reasonable estimate. Further, polynomial fitting
79 correlation between wave, current, and total shear stress with SSC was put forwarded by
80 researchers(Tang et al. 2020; Wu et al. 2013), but showed discriminatory for the different study
81 regions and analysis methods. The relationship between SSC and wind condition was disclosed then
82 through field investigation and statistic analysis, which was further applied to prediction model.
83 However, it was unable to explain the inherent mechanism of wind condition on SSC variation, while
84 the contribution of sediment suspension and migration for local sediment concentration was
85 significant for further measures of turbidity reducing. Furthermore, sediment sampled from the
86 collection site has difficulty maintaining the original characteristics, and the conditions in the
87 laboratory are all simplified, thus causing great deviations from the practical conditions.

88 Numerical simulation was then commonly used to imitate the hydrodynamics and sediment field
89 of the entire lake (Qiu et al. 2013; Li 2016). Models covering the entire water surface take more actual
90 factors into consideration, such as boundary conditions and sediment transportation, which are all
91 crucial for sediment processes. But model results from simulations have always been used to analyze
92 the spatial response of sediment under wind action but are seldom related to turbidity forecast.
93 Because turbidity is affected by physical, chemical, and biological factors, describing it quantitatively
94 as well as accurately predicting it is difficult. Techniques from the field of machine learning, such as
95 artificial neural networks (ANNs) (Kennedy et al. 2015), genetic algorithms (GAs) (Burchard-Levine
96 et al. 2014; Aani et al. 2019), and support vector machines (SVMs) (Wang et al. 2009) have also been
97 used in water quality prediction, for its outstanding ability in handling the nonlinear information. But
98 it also has the problem of interpretability.

99 Thus, hydrodynamic and sediment transport models driven by wind fields from MIKE 21/3
100 software and the recorded high-frequency turbidity data of raw water were used in the current study
101 to: (1) observe the impact of wind speed and direction on hydrodynamic and sediment distribution of
102 the lake; (2) investigate the effect of wind on SSC variation in the study site, and explain the respective
103 contribution of sediment resuspension and migration to it; (3) study the response intensity of
104 simulated SSC on turbidity and explore the potentiality of long-term turbidity prediction based on
105 numerical simulation.

106 **2 Methods and Models**

107 **2.1 Study area**

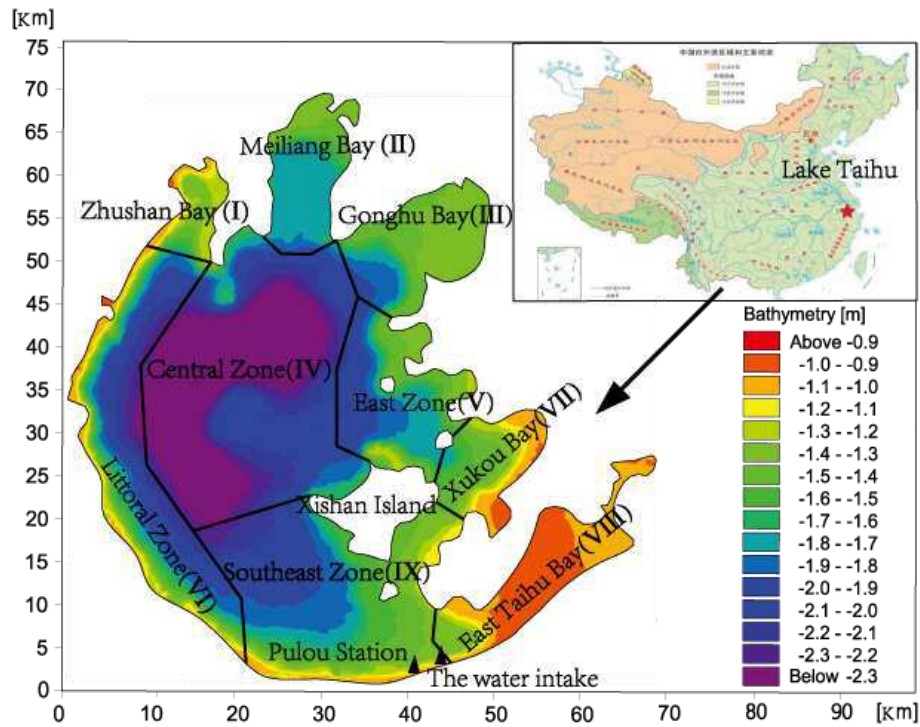
108 Lake Taihu (30°56'~31°33' N and 119°53'~120°36' E) located in the lower Yangtze delta (Fig.

109 1) is the third largest freshwater lake in China. It has a water surface area of 2388.1 km² and a mean
110 depth of 1.9 m, and has become an important drinking water source for 38 cities (population
111 coverage of approximately 60 million). The city of Huzhou, Zhejiang Province is one of the
112 beneficiaries. The Taihu waterworks located here pump raw water from east Taihu Lake through
113 two 7.6-kilometer-long diversion pipes, and the water-supply covers more than 400 square
114 kilometers and over one million residents. The water intake (Fig. 1) is close to the bank with an
115 average water depth of approximately 1 m. The shallowness makes it easier for wind-induced
116 waves and currents to cause intense hydrodynamic disturbance in the water body, and further
117 turbidity increases at the study site. The dramatic fluctuation of the influent turbidity has resulted
118 in problems for waterworks management.

119 It should be noted that, other meteorological factors like air temperature and rainfall may play a
120 part as well (Zhang et al. 2021). However, the former primarily contributed to turbidity caused by
121 biological and chemical factors rather than sediment movement. And the latter mainly function
122 through water level, quality and pollutant flux of inflow and outflow rivers to the lake, surface
123 runoff. It has been proved that the flow structure of the lake was less sensitive to water level and
124 inflow/outflow for the large area and the flat terrain (Qin et al. 2005). In addition, there was
125 approximately 10 km away from the closest inlet (Taipu river) to the water intake area, that made
126 the change of sediment flux due to rainfall less influential to the study area. And the surface runoff
127 was filtered and intercepted since the coast of the site was relative gradual and covered with
128 vegetation, the effect of it to SSC in study area became unconsidered then.

129 Therefore, this study is devoted to investigating how wind fields affect the turbidity of raw water

130 and exploring the potentiality of turbidity prediction based on field simulation. The meteorological
131 station closest to the water intake, Pulou (30°56'00" N, 120°17'57" E) station, was selected as the
132 observation site (Fig.1).



133
134 **Fig. 1** Location and Bottom elevation of Lake Taihu with observation site

135 2.2 Data collection

136 The wind field data (wind speed, wind direction) of Pulou Station were provided by the Huzhou
137 Meteorological Observatory of Zhejiang Province with an interval of 1 h. Historical turbidity data
138 were acquired from Taihu Waterworks. Hourly data of the raw water pumped from the water intake
139 were automatically recorded by a Hach online turbidity. In addition, the cyanobacteria concentration
140 of the water intake area with an interval of 4 h was also collected from the Huzhou Environmental
141 Monitoring Center to observe the contribution of algae to the turbidity. All real time datasets used in
142 this study were from January 1, 2020, to December 31, 2020.

143 **2.3 Modeling**

144 2.3.1 Governing Equations

145 MIKE 3 has been widely used in areas such as oceans, coastal regions, estuaries, and lakes,
146 which uses incompressible Reynolds-averaged Navier–Stokes equations and adopts the Boussinesq
147 approximation and hydrostatic assumption (Huang et al. 2013). This study used MIKE 3 to set up
148 numerical simulation models to analyze the waves, flows and sediment pattern of Lake Taihu under
149 diversified wind conditions. By considering the dominant force and type of sediment in the lake, the
150 following modules were selected: the HD (hydrodynamic) and the MT (mud transport) modules from
151 the MIKE 3 software package, and the SW (spectral waves) module from the MIKE 21/3 software
152 package. The HD module and SW module achieved bidirectional coupling by sharing hydrodynamic
153 information obtained in the HD module and the wave factors calculated in the SW module (Kuang et
154 al. 2016). The MT module is linked to the 2D wave module (SW) and 3D hydrodynamic model of
155 the current (HD), and uses modeled data for the calculation of sedimentation processes
156 simultaneously.

157 The SW model bases on unstructured meshes, and the fully spectral formulation was adopted in
158 this study. The wave action balance equation is described as follows (Komen et al. 1994).

$$N(\sigma, \theta) = E(\sigma, \theta) / \sigma \quad (1)$$

159 where N is the action density, E is the energy density, θ is the wave component direction ($^\circ$), and
160 σ is the relative angular frequency (r/s), the spectrum is limited to the range between a minimum
161 (σ_{min}) and maximum (σ_{max}) value.

162 The evolution of the wave spectrum in position (x, y) and time (t) (Hasselmann et al. 1973) is:

$$\frac{\partial}{\partial t} N + \frac{\partial}{\partial x} C_x N + \frac{\partial}{\partial y} C_y N + \frac{\partial}{\partial \sigma} C_\sigma N + \frac{\partial}{\partial \theta} C_\theta N = \frac{S_{SW}}{\sigma} \quad (2)$$

$$(C_x, C_y) = \frac{d\vec{x}}{dt}, \quad C_\sigma = \frac{d\sigma}{dt}, \quad C_\theta = \frac{d\theta}{dt} \quad (3)$$

163 where $\vec{x} = (x, y)$ is the Cartesian co-ordinates; C_x, C_y, C_σ , and C_θ are the propagation velocities in
 164 x, y, σ and θ space, respectively; S_{SW} is the source term for the energy balance equation. The
 165 radiation stresses, S_{xx}, S_{xy}, S_{yx} and S_{yy} (m^3/s^2), significant wave height, H_s (m) and zero-crossing
 166 wave period T_z (s) used in HD model are derived from SW model:

$$H_s = \sqrt{E} \quad (4)$$

$$T_z = \sqrt{E / \left(\int_0^{2\pi} \int_0^{\sigma_{max}} E(\sigma, \theta) \sigma^2 d\sigma d\theta + \frac{\sigma_{max}^3}{2} \left[\int_0^{2\pi} E(\sigma_{max}, \theta) d\theta \right] \right)} \quad (5)$$

$$S_{xx} = \frac{1}{2} g \left(\int_0^{2\pi} \int_0^\infty \left(\cos^2 \left(\frac{3}{2} \pi - \theta \right) + 1 \right) \left(1 + \frac{2kh}{\sinh(2kh)} \right) E(\sigma, \theta) d\sigma d\theta \right) \quad (6)$$

$$S_{xy} = S_{yx} = \frac{1}{2} g \left(\int_0^{2\pi} \int_0^\infty \cos \left(\frac{3}{2} \pi - \theta \right) \sin \left(\frac{3}{2} \pi - \theta \right) \left(1 + \frac{2kh}{\sinh(2kh)} \right) E(\sigma, \theta) d\sigma d\theta \right) \quad (7)$$

$$S_{yy} = \frac{1}{2} g \left(\int_0^{2\pi} \int_0^\infty \left(\sin^2 \left(\frac{3}{2} \pi - \theta \right) + 1 \right) \left(1 + \frac{2kh}{\sinh(2kh)} \right) E(\sigma, \theta) d\sigma d\theta \right) \quad (8)$$

167 Where k is the wave number; h is the full water depth (m).

168 The local continuity equation in HD model is written as Eq.9, and the two horizontal momentum
 169 equations for the x- and y- component are described as Eq.10 and Eq.11, respectively. Based on the
 170 hydrostatic approximation in vertical direction, the equation degenerated into Eq.10:

$$\frac{\partial u}{\partial x} + \frac{\partial v}{\partial y} + \frac{\partial w}{\partial z} = S_{HD} \quad (9)$$

$$\frac{\partial u}{\partial t} + \frac{\partial u^2}{\partial x} + \frac{\partial vu}{\partial y} + \frac{\partial wu}{\partial z} =$$

$$fv - g \frac{\partial \zeta}{\partial x} - \frac{1}{\rho_0} \frac{\partial p_a}{\partial x} - \frac{g}{\rho_0} \int_z^\zeta \frac{\partial \rho}{\partial x} dz - \frac{1}{\rho_0 h} \left(\frac{\partial S_{xx}}{\partial x} + \frac{\partial S_{xy}}{\partial y} \right) + F_u + \frac{\partial}{\partial z} \left(\mu_v \frac{\partial u}{\partial z} \right) + u_s S_{HD} \quad (10)$$

$$\frac{\partial v}{\partial t} + \frac{\partial v^2}{\partial y} + \frac{\partial uv}{\partial x} + \frac{\partial wv}{\partial z} =$$

$$fu - g \frac{\partial \zeta}{\partial y} - \frac{1}{\rho_0} \frac{\partial p_a}{\partial y} - \frac{g}{\rho_0} \int_z^\zeta \frac{\partial \rho}{\partial y} dz - \frac{1}{\rho_0 h} \left(\frac{\partial S_{yx}}{\partial x} + \frac{\partial S_{yy}}{\partial y} \right) + F_v + \frac{\partial}{\partial z} \left(\mu_v \frac{\partial v}{\partial z} \right) + v_s S_{HD} \quad (11)$$

$$\frac{\partial p_a}{\partial z} = -\rho g \quad (12)$$

171 Where t is time (s); ζ is the water elevation (m), d is the still water depth (m), $h = \zeta + d$;
 172 u, v, w are velocity components in the x, y , and z directions, respectively (m/s); f is the
 173 Coriolis parameter (s^{-1}); ρ is the density of the water (kg/m^3) and ρ_0 is the reference density
 174 (kg/m^3); μ_v is the vertical eddy viscosity (m^2/s); p_a is atmospheric pressure (Pa); g is
 175 gravitational acceleration (m/s^2); S_{HD} is the source term and u_s and v_s are the velocity components
 176 at which the source water enters the adjacent part. The terms of horizontal stress F_u, F_v can be
 177 described using the gradient stress, which is simplified to:

$$F_u = \frac{\partial}{\partial x} \left(2\mu_h \frac{\partial u}{\partial x} \right) + \frac{\partial}{\partial y} \left(\mu_h \left(\frac{\partial u}{\partial y} + \frac{\partial v}{\partial x} \right) \right) \quad (13)$$

$$F_v = \frac{\partial}{\partial x} \left(\mu_h \left(\frac{\partial u}{\partial y} + \frac{\partial v}{\partial x} \right) \right) + \frac{\partial}{\partial y} \left(2\mu_h \frac{\partial v}{\partial y} \right) \quad (14)$$

178 where μ_h is horizontal eddy viscosity.

179 The surface (at $z = \zeta$, Eq.6) and bottom (at $z = -d$, Eq.7) boundary condition for u, v, w
 180 are determined by surface wind stress ($\vec{\tau}_s$) and bottom stress ($\vec{\tau}_b$):

$$\frac{\partial \zeta}{\partial t} + u \frac{\partial \zeta}{\partial x} + v \frac{\partial \zeta}{\partial y} - w = 0, \quad \left(\frac{\partial u}{\partial z}, \frac{\partial v}{\partial z} \right) = \frac{1}{\rho_0 \mu_v} \vec{\tau}_s \quad (15)$$

$$u \frac{\partial d}{\partial x} + v \frac{\partial d}{\partial y} + w = 0, \quad \left(\frac{\partial u}{\partial z}, \frac{\partial v}{\partial z} \right) = \frac{1}{\rho_0 \mu_v} \vec{\tau}_b \quad (16)$$

181 The stress is given by the following relation:

$$\vec{\tau}_s = \rho_a c_d |u_w| \vec{u}_w \quad (17)$$

$$\vec{\tau}_b = \vec{\tau}_c + \vec{\tau}_w = 0.5\rho(f_c|U|\vec{U} + f_w|U_b|\vec{U}_b) \quad (18)$$

$$U_b = \frac{2H_s}{T_z} \frac{1}{\sinh(2\pi h/L)} \quad (19)$$

$$L = \frac{gT_z^2}{2\pi} \left(\tanh \left[\frac{2\pi}{T_z} \sqrt{\frac{h}{g}} \right] \right)^{3/2} \quad (20)$$

182 Where ρ_a is the density of air (kg/m³); c_d is the drag coefficient of wind depended on the wind
 183 speed; \vec{u}_w is the wind velocity (m/s); $\vec{\tau}_c$ and $\vec{\tau}_w$ are the shear stress induced by currents and waves,
 184 respectively; f_c and f_w are the current and wave friction factors determined by bed roughness k_s ;
 185 U is the horizontal current velocity (m/s); U_b is the horizontal wave orbital velocity at the bed (m);
 186 L is the wave length (m).

187 The cohesive sediment transport was modeled using the Mud Transport module (MIKE 3 MT).

188 The term of mud is generally used for fine-grained and cohesive sediment with grain sizes less than
 189 0.063 mm. The module is based on the advection-dispersion equation:

$$\frac{\partial c}{\partial t} + u \frac{\partial c}{\partial x} + v \frac{\partial c}{\partial y} = \frac{\partial}{\partial x} (D_x \frac{\partial c}{\partial x}) + \frac{\partial}{\partial y} (D_y \frac{\partial c}{\partial y}) + \frac{\partial}{\partial z} (D_z \frac{\partial c}{\partial z}) + S_{MT} + S_E + S_D \quad (21)$$

190 Where c is the SSC (kg/m³); D_x , D_y , and D_z are dispersion coefficients (m²/s); S_{MT} is source term;
 191 S_D , S_E are the deposition and erosion terms (kg/m³/s). The deposition rate S_D can be expressed by
 192 Eq.22, and the erosion rate for dense, consolidated bed and soft, partly consolidated bed are defined
 193 by Eq.23 (Partheniades 1965) and Eq.24 (Parchure and Mehta 1985), respectively:

$$S_D = w_s c_b \left(1 - \frac{|\vec{\tau}_b|}{\tau_{cd}} \right) \quad (22)$$

$$S_E = Q \left(\frac{|\vec{\tau}_b|}{\tau_{ce}} - 1 \right)^n \quad (23)$$

$$S_E = Q \exp \left[\alpha (\tau_b - \tau_{ce})^{1/2} \right] \quad (24)$$

194 Where w_s is the settling velocity of each sediment fraction (m/s); c_b is the near bed concentration
 195 (kg/m^3) that proportional to c ; τ_{cd} and τ_{ce} are the critical shear stress for deposition and erosion
 196 (N/m^2); Q is the erodibility of bed ($\text{kg/m}^2/\text{s}$); n and α are the power of erosion for dense and soft
 197 bed, respectively. Additionally, the dry density of the bed ρ_b is also needed to refresh the bed
 198 thickness during calculating.

199 The MIKE 3 model solves the integrated equations of mass conservation and momentum
 200 conservation in space and time using explicit and implicit alternating techniques. The solution of each
 201 direction and individual grid are achieved by applying the double precision scanning method.

202 2.3.2 Grid generation

203 To simulate the hydrodynamic and sediment action of Lake Taihu by the MIKE 21/3 model,
 204 determining the exact bathymetric data of the lake was considered the most basic step. The water
 205 depth (z) data were obtained from the work of Qiu et al. (2013), a measurement performed in 2009
 206 covering 69×69 sampling points of the whole lake. The xyz file for land area was then created and
 207 fed as input to MIKE 21/3 software to calculate depth contours for the model domain. As shown in
 208 Fig. 1, the lake center has the largest depth of 2.4 m, while the eastern part is relatively shallow.

209 An unstructured triangle grid was created by mesh generator module in MIKE zero. In the
 210 horizontal direction, a nested grid was adopted by applying triangulation parameters with a maximum
 211 element area of 400000 m^2 and a maximum number of nodes 100000 for the regional model (the

212 whole lake). The local model zooms on the area around the water intake with a maximum element
213 area of 80000 m², and the minimum side length of the grid is approximately 100 m. In this way, the
214 boundaries of the local model are given by the corresponding calculated data from the regional model,
215 which can make the simulation results more accurate. The σ -average layer was used in the vertical
216 direction. Because of the shallowness of the lake, 5 uniform layers were considered adequate to
217 resolve the structures. Imported bathymetric values were then interpolated to cover each grid and
218 mesh. The finally developed mesh consisted of 51275 nonoverlapping elements, and 33036 nodes.

219 **2.4 Calibration**

220 Before application, the model was calibrated by modifying the coefficients empirically or
221 through measurements to fit the situation of the study area. Due to the lack of field measurements
222 that are supposed to cover the entire lake, the results from the work of Zhao Q. et al (2018) were used
223 to calibrate and obtain the best performance of the developed model in this paper. They simulated the
224 flow, wave height and sediment concentration distribution of Lake Taihu under steady wind action
225 (SW wind of 9 m/s and 12 m/s) by the MIKE DHI software, a similar method as the current study.

226 For the HD module, there are 3 main influencing coefficients: the (horizontal/vertical) eddy
227 viscosity coefficient, the bed resistance coefficient, and the wind friction coefficient. The horizontal
228 and vertical eddy viscosities were determined through the Smagorinsky formulation and constant
229 eddy formulation, respectively. The coefficients in previous work varied widely with a range of
230 0.001~5 (Shu et al. 2021; Tang et al. 2011), and the determined values of 0.28 for horizontal and 0.3
231 for vertical were finally obtained to be optimal. The bed resistance was described by the Manning
232 number and set as a constant of 31 m^{1/3}/s in the domain after calibration. The wind friction coefficient

233 varied linearly with wind speed: high values often lead to good performance with strong winds, while
234 for weak winds, smaller coefficients should be used, and the default values were adopted here. The
235 initial surface elevation was set as 0 m for all working conditions , that is, the initial water depth was
236 equal to the bottom elevation. Because the water level of Lake Taihu has a small fluctuation within
237 30 cm (Xu et al. 2020), it was reasonable to leave out the impact of it on sediment distribution. The
238 SW model operates based on fully spectral formulation to achieve wind-wave growth, and the most
239 influential factor, bottom friction, was expressed by the Nikuradse roughness, which was 0.03
240 according to the model performance. The limitation of wave frequency and wave breaking coefficient
241 were set as default, and the influence of white capping was ignored due to the relatively weak effect
242 in shallow water bodies.

243 The hydrodynamic information from the HD and SW simulations was directly used in the MT
244 model. For this part, the sediment parameters set in the MT model were closely related to the
245 simulation results, including the number of bed layers and sediment fractions, settling velocity,
246 critical shear stress, density and thickness of layers. These parameters were referred in previous works
247 conducted in Lake Taihu. Qin et al (2007) investigated the spatial distribution of sediments at 723
248 sites and found that sediment covers approximately 45% of the lake area with a depth of 0.6~5.5 m,
249 and mass exchange in the water-sediment interface exists mainly within the top 5~10 cm (Qin et al.
250 2004; Luo et al. 2004). The unconsolidated sediment was mainly concentrated in the northwestern
251 and southeastern sections (VI and IX) of the lake, whereas the consolidated sediment was primarily
252 confined to the central region (IV) which was frequently disturbed by wind-induced waves (Wu et al.
253 2018). Thus, 2 bed layers were set in the MT model, with a constant thickness of 0.1 m for the weak

254 fluid mud layer (layer 1) and spatial variation for the fluid mud layer (layer 2, [Online Resource 1](#)).

255 The dry densities of the bed material were 180 and 320 kg/m³ respectively according to the geological

256 properties. The primary parameters for the erosion process occurring in the bottom layer were the

257 critical shear stress and erosion coefficient, which were taken as 0.05 N/m² and 0.00002 for layer 1

258 and 0.1 and 0.0001 for layer 2 on the basis of previous studies ([Luo et al. 2004](#)). Works on sediment

259 granulometric composition conducted in Lake Taihu revealed that the particle size ranged from 0.002

260 to 0.14 mm, the media size was approximately 0.008 mm, and sediments with particle sizes below

261 0.02 mm (i.e., silt and clay) accounted for approximately 80% ([Hu et al. 2006](#); [Hou et al. 2013](#)).

262 Therefore, the sediments were divided into 2 fractions, and characterized by mean settling velocity

263 and critical shear stress. The settling velocity is dependent on the size of the particles and can be

264 roughly estimated through Stokes law ([Brun-Cottan, 1976](#)):

$$w_s = \frac{\rho_s - \rho}{\rho} \frac{gd^2}{18 \cdot \nu} \quad (25)$$

265 Where, ρ_s is sediment density ranged in 1600 ~ 1700 kg/m³ and took 1600 kg/m³ here; ρ is

266 the density of water; g is the gravity (9.82m/s²); ν is the viscosity (here was 1.01×10^{-6} m²/s); d is

267 grain size (m), and took 0.008 mm and 0.02 mm for fractions 1 and 2, respectively, and the

268 corresponding mean settling velocity were 0.00002 m/s and 0.00015 m/s.

269 The critical shear stress for deposition is generally a calibration parameter, and normal values

270 are in the interval 0~0.1 N/m², but no larger than 0.3. By referring to previous experiments ([Qiu et al.](#)

271 [2013](#); [Pang et al. 2006](#)) and “trial-and-error”, the values were set as 0.03 N/m² and 0.05 N/m² for

272 fractions 1 and 2.

273 The comparison between the modeling results by the effect of SW wind (9 m/s) is shown in

274 [Online Resource 2](#), and their agreement was satisfied in general, especially for current speed and
 275 significant wave height. A smaller discrepancy in sediment distribution was observed, which may be
 276 attributed to the setting of layer thickness, Zhao et al. (2018) adopted a uniform sediment layer,
 277 whereas the current model considered spatial discrepancy. The heavy unconsolidated bed layer near
 278 Xishan Island conveyed a great deal of sediment to the center during southwesterly wind events,
 279 consequently engendered higher concentrations in northern Taihu Bay than in East Taihu Bay (VIII).
 280 The primary parameters determined after calibration are summarized in [Table 1](#).

281 **Table 1 Model parameters**

Model	Parameters	Value
HD Model	Bed resistance (Manning number)	31 (m ^{1/3} /s)
	Horizontal eddy viscosity coefficient (μ_h)	0.28 m ² /s
	Vertical eddy viscosity coefficient (μ_v)	0.3 m ² /s
	Wind friction coefficient (c_d)	0.001255(at 7 m/s)~ 0.002425(at 25 m/s) (default)
	Coriolis parameter (f)	Vary in domain
	Initial surface elevation	0 (m)
	Initial $u/v/w$ -velocity	0.01 (m/s)
SW Model	Minimum frequency (σ_{min})	0.05 (Hz, default)
	Maximum frequency (σ_{max})	0.4 (Hz, default)
	Wave breaking (constant Gamma data)	0.8 (default)
	Bottom friction (constant Nikuradse roughness, k_s)	0.03
MT Model	Number of fractions	2
	Number of layers	2
	Thickness of layer 1	0.1 (m)
	Thickness of layer 2	Online Resource1
	Proportion of fraction 1 in layer 1 & 2	0.8
	Proportion of fraction 2 in layer 1 & 2	0.2
	Mean settling velocity of fraction 1 (w_{s1})	0.00002 (m/s)
	Mean settling velocity of fraction 2 (w_{s2})	0.00015 (m/s)
	Critical shear stress for deposition of fraction 1 (τ_{cd1})	0.03 (N/m ²)
	Critical shear stress for deposition of fraction 2 (τ_{cd2})	0.08 (N/m ²)
Critical shear stress for erosion of layer 1 (τ_{ce1})	0.05(N/m ²)	
Critical shear stress for erosion of layer 2 (τ_{ce2})	0.1(N/m ²)	

Erosion coefficient of layer 1 (Q_1)	0.00002
Erosion coefficient of layer 2 (Q_2)	0.0001
Dry density of bed layer1 (ρ_{b1})	180 (kg/m ³)
Dry density of bed layer2 (ρ_{b2})	320 (kg/m ³)
Horizontal dispersion coefficient of fraction 1 & 2 (D_x , D_y)	0.8 m ² /s
Vertical dispersion coefficient of fraction 1 & 2 (D_z)	1 m ² /s
Power of erosion for bed layer 1 (α)	4
Power of erosion for bed layer 2 (n)	1
Initial concentration of fraction 1 & 2	0.01 (kg/m ³)

282 3 Working conditions setting

283 Wind field data were processed through classification, wind speed was separated into 12
284 intervals from 0~12 by increments of 1 m/s and larger than 12 m/s, and wind directions were divided
285 into 16 intervals. The seasonal characteristics of the wind field were also considered. Five wind rose
286 diagrams are shown in Fig.2, each was characterized by frequency appearance, and labels close to the
287 petals show the mean wind speed of the subdataset within this part. The wind direction was also
288 presented onshore, offshore and alongshore according to the direction of the shoreline of the water
289 intake area.

290 For 2020, there were 4 main wind directions (ESE, SE, SSE, NNW) accounting for 38.1% (9.9%,
291 10.4%, 8.9%, 8.9%, respectively) with mean speeds of 2.4, 1.8, 2.0, and 4.8 m/s, followed by S (7.7%),
292 NW (7.7%), NE (7.0%), E (7.0%), N (6.8%), and NNE (6.7%). The median speed was approximately
293 3 m/s; intervals of 0~3 m/s occupied 54.7% of all samples, and 98.3% were below 8 m/s. More
294 precisely, most of the strong winds were found in onshore winds (WNW, NW, NNW) which
295 contributed 20.8% of the year. Weaker winds were strongly related to offshore wind directions (ESE,
296 SE, SSE), which accounted for 29.1%. The characteristics of the winds of the study area provided
297 diversification from one season to another. During winter, onshore winds with average speeds of

298 4.3~4.9m/s primarily prevailed over Lake Taihu, and the dominant wind was in the NNW direction
299 associated with a relatively strong force. For summer, offshore winds led with an average speed of
300 2.0~2.7m/s, and the main wind of SSE was characterized by low speed. For the other months, the
301 wind fields seemed to be less concentrated because multiple dominant wind directions were found
302 during this period. In spring, the winds came from the east and south with mean speeds varying
303 principally between 1.6 and 2.9 m/s. The winds in fall were mostly northerly, with mean speeds
304 ranging from 3.3 to 4.7 m/s.

305 Overall, the wind fields at Lake Taihu changed dramatically with the speed from calms (<0.1
306 m/s) to a maximum of 13.2 m/s, and the wind directions were scattered as well. Therefore, 192 models
307 driven by wind forces covering all regimes (12 speed intervals of 1 m/s and 16 direction intervals,
308 cases of wind speeds >12 m/s were neglected for the extremely low proportion, which accounted for
309 only 0.15% of all samples) were built to achieve a comprehensive investigation of sediment dynamics
310 behavior under diversiform wind conditions in the water intake area. Considering that the water intake
311 area is shielded from southeasterly winds but exposed to long fetches for winds from the north or
312 west, typically cases of onshore (NNW), offshore (SSE) and alongshore (ENE and WSW) winds at 3
313 m/s and 8 m/s were taken as analysis objects to observe both the combined and separate effects of
314 wind speed and direction on the sediment distribution of the lake in detail.

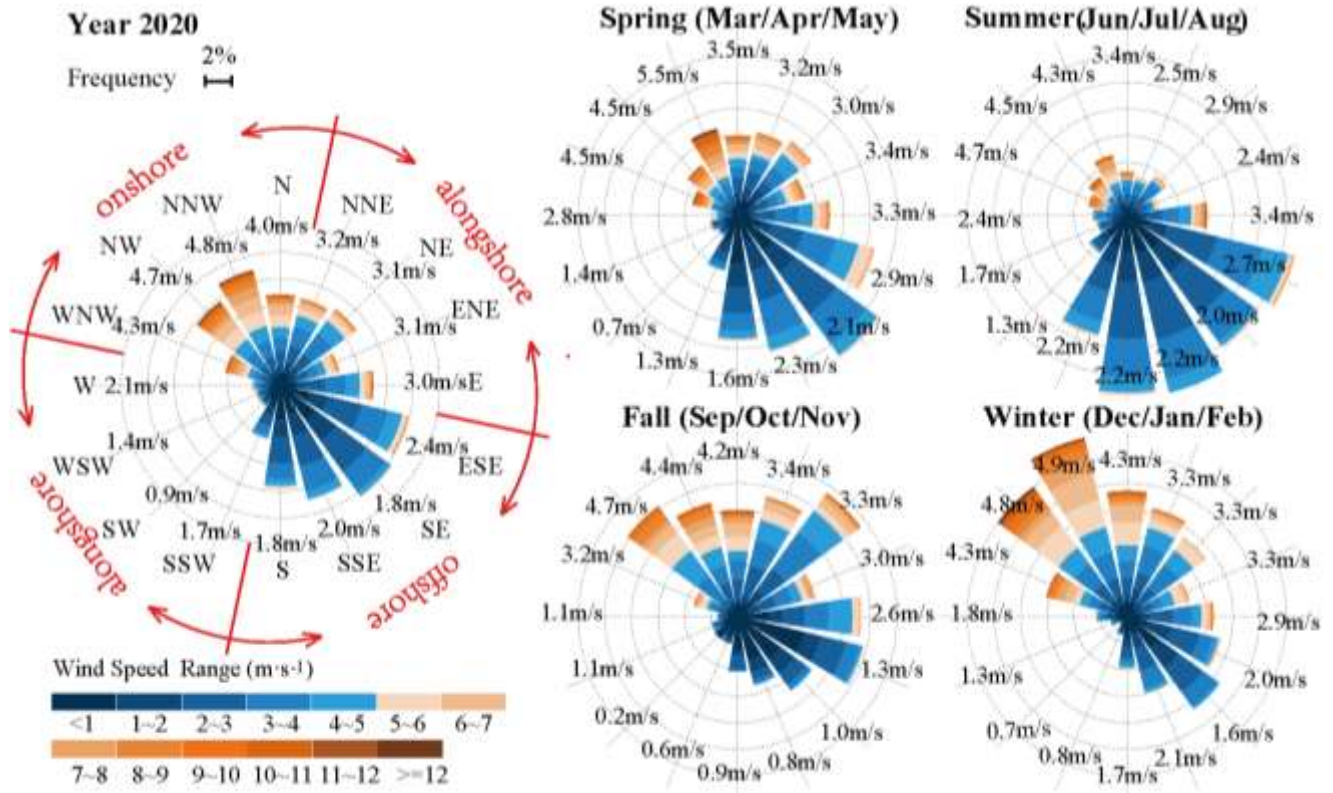


Fig. 2 Wind conditions of the year 2020

4 Results and discussion

4.1 The effect of wind fields on sediment distribution

As shown in Figs. 3a and 4a, the final stable wind-current distributions were the combination of circulations and alongshore currents. The patterns of inversed winds were extremely similar but with inversed rotation gyres, which resulted from the bottom topography (Luo et al. 2003). The current speed sharply increased in response to the enhanced wind force. Generally, the alongshore currents parallel to the wind direction acquired relatively high speeds because less energy was absorbed by boundaries, and semiclosed bays obtained extremely calm flow correspondingly. Circulations were subject to form at the lake shores, with counterclockwise gyres mainly generated at the windward shores, whereas reverse gyres were more likely to be generated at the leeward. For the NNW and SSE

327 winds (Fig. 3a), the maximum flow rate was displayed at the southwest shore for the long lake
328 shoreline over 20 km, with values of approximately 0.02 m/s and 0.1 m/s at the wind speeds of 3 m/s
329 and 8 m/s, respectively. When the lake experienced WSW and ENE winds, the highest values
330 (approximately 0.03 m/s and 0.09 m/s at the wind speeds of 3 m/s and 8 m/s, respectively) occurred
331 in the narrow areas before the mouth of the Xukou Bay.

332 Wind waves grew higher following the increase in wind force as well, with greater friction drag
333 delivering more energy into the water through turbulence and then dissipated by bottom friction. The
334 propagation direction of the wind waves was almost consistent with the wind direction (Figs. 3b and
335 4b). Waves increased from the windward shoreline to the open water, being much higher than those
336 at leeward shores when less wind energy (at the wind speed of 3 m/s) was conveyed into water. The
337 significant wave height was induced by water level oscillations, and their distribution patterns are
338 related to the wind fetch (the horizontal distance that wind continues to blow across the water surface).
339 Long fetches helped with wave growth, and wind speed significantly impacted the wave motion in
340 the lake (Zheng et al. 2015). However, waves achieved fun growth when the wind speed reached 8
341 m/s, and the central region obtained largest wave height (above 0.32 m) then because of the relatively
342 wide surface and deep depth.

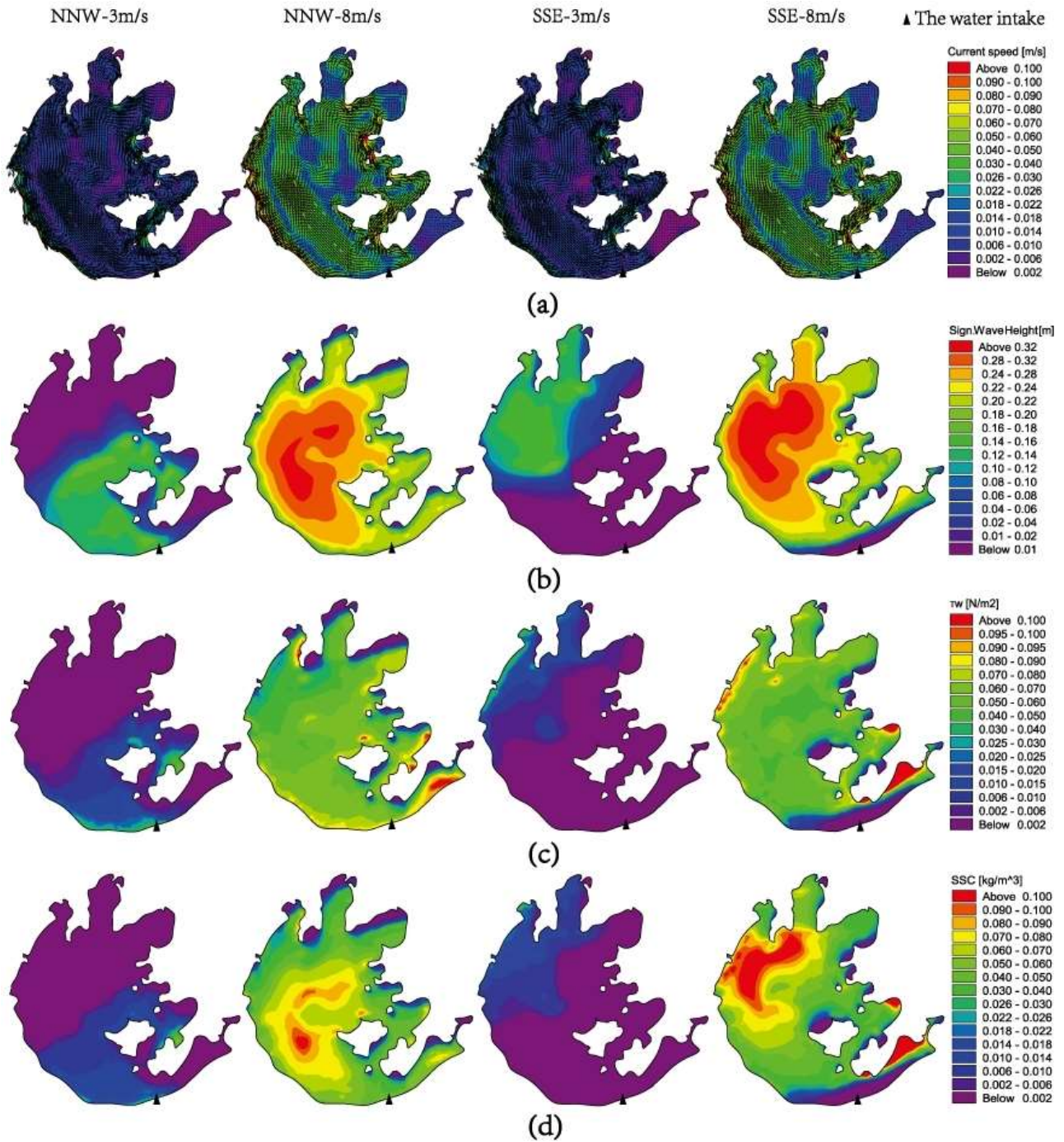
343 Overall, onshore strong winds can effectively activate higher wave shear stress, whereas lower
344 offshore winds contributed less to its generation (Figs. 3c and 4c). Once the threshold stress is
345 exceeded, sediment particles can be triggered and enter the overlying water body, thus leading to an
346 increase in SSC values. In contrast, waves are of low energy with very low suspension potential. The
347 corresponding sediment fields are presented in Figs. 3d and 4d, which show that wind direction has

348 a pronounced influence on sediment dispersal. It determined the direction and efficiency of the
349 propagation, whereas wind strength affected the spatial intensity. Analogous patterns of shear stress
350 and SSC at a wind speed of 3 m/s within the same direction may be ascribed to the particularly low
351 potential of sediment transportation. With a light wind, the shear stress induced by waves ranged from
352 0 to 0.06 N/m² and was below 0.01 N/m² in most areas, which was lower than the critical value
353 triggering sediment resuspension (Li 2016; Qin 2004; Luetlich R.A. et al. 1990). This made fewer
354 particles suspended, and thus transportation played a negligible role in sediment redistribution. As
355 the wind speed increased, more energy was delivered to hydrodynamic processes (waves and
356 currents), the shear stress distribution went through the microscale to the entire lake and the critical
357 shear stress at the upper limit of 0.06kg/m³ (with the range of 0.02~0.06 kg/m³ indicated by previous
358 studies) was exceeded for almost the whole area. Deviations between shear stress and sediment
359 patterns were then observed, especially in the central region.

360 Due to the short distance between the water intake and the lake shore, the local SSC was
361 impacted significantly by the resistance from the shore, particularly with the typical conditions of
362 onshore (NNW) and offshore (SSE) winds. The water intake area was exposed to long fetches and
363 suffered from high waves in the case of NNW winds, and the activated waves efficiently motivated
364 the sediment and promoted particle entrainment. Because the abundant lakebed deposits in the
365 southeastern part of the lake enabled sediment to easily enter the overlying water body by wave
366 disturbance, particles suspended in that area were then conveyed into the observed site along with the
367 southeastern wind currents. Both the effect of suspension and transportation helped to develop high
368 SSC when the lake went through northwesterly winds, which caused the low incipient wind speed (<

369 3 m/s) for SSC to increase at the water intake area. The circulation formed here by the resistance of
370 the lakeshore hindered movement and deposition of the suspended sediment, providing the conditions
371 for maintenance of high SSC values. A similar process was appeared under SSE winds, which led to
372 high SSC at the northwestern shore of East Taihu Bay and the northwestern section of the lake (IV
373 and VI), but extremely low SSC values at the study site instead.

374 By the effect of alongshore winds, the southeastern lake was confronted by a short wind fetch
375 that was adverse to the development of waves. The tiny shear stress generated at the site by the wind
376 speed of 3 m/s failed to trigger deposits, thus, higher energy was required for the incipient motion of
377 the SSC increase compared to the northwesterly wind. Because most regions achieved the critical
378 shear stress in response to the increased wind force, the sediment was stimulated. Suspended particles
379 at East Taihu Bay (VIII) moved toward the water intake area first by the ENE wind, and the followed
380 inverse compensating currents carried sediment from the littoral zone (VI) to the site then,
381 consequently causing an increase in SSC. Approximate progress was developed under the condition
382 of WSW wind, and sediment was transported from the littoral zone at first and then the Bay instead.
383 Seeing that the observed site was at the mouth of the bay and a large amount of sediment was directly
384 transported here, the local SSC may be higher than that under onshore conditions with the same wind
385 speed.



386

387

Fig. 3 Field distributions at the speed of 3m/s and 8m/s under NNW and SSE winds:

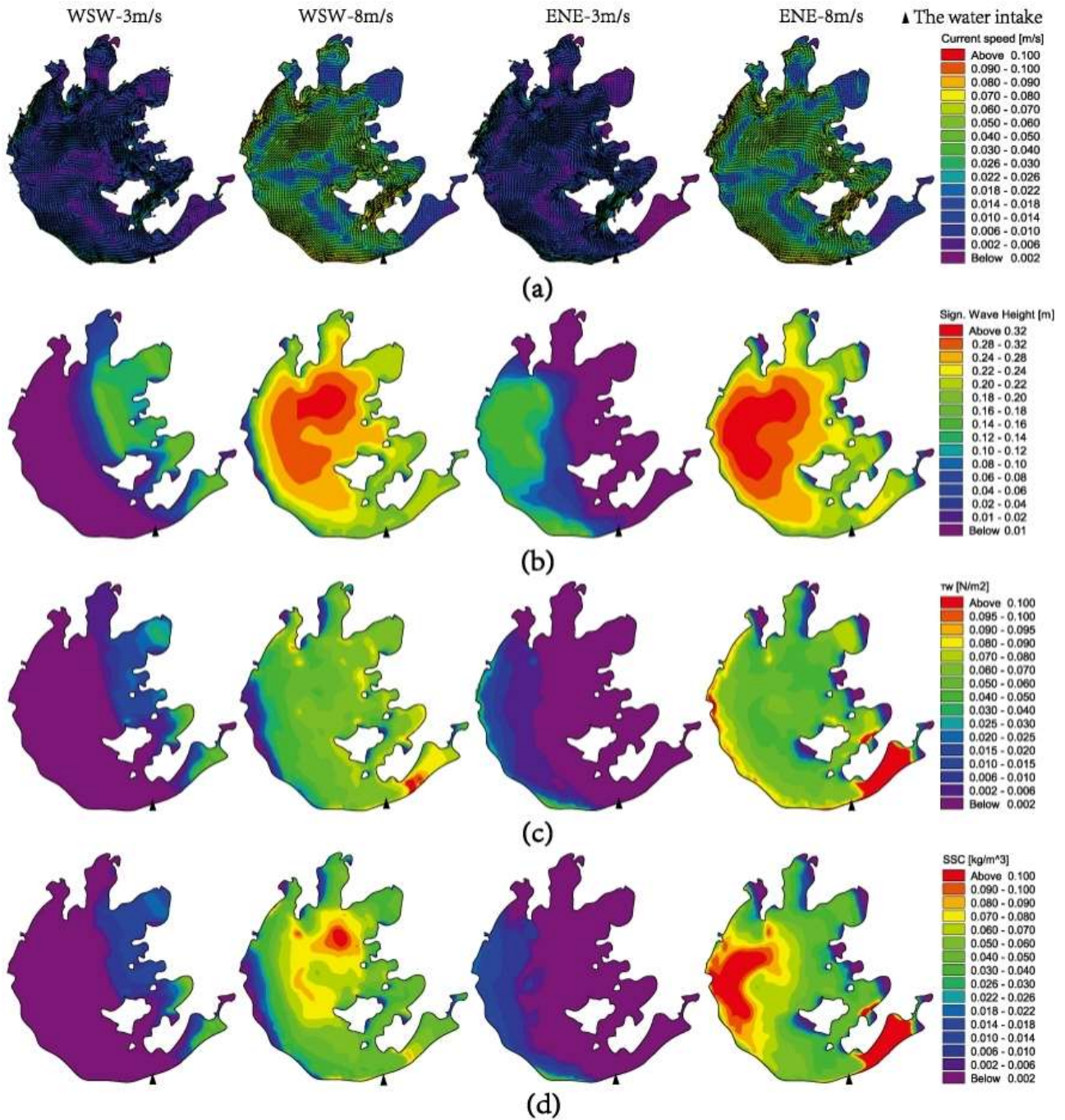
388

(a) Current; (b) Significant wave height; (c) wave induced shear stress; (d) SSC

389

390

391



393

394

Fig. 4 Field distributions at the speed of 3m/s and 8m/s under WSW and ENE winds:

395

(a) Current; (b) Significant wave height; (c) wave induced shear stress; (d) SSC

396

The steady values of simulated SSC at the water intake under different model conditions are

397

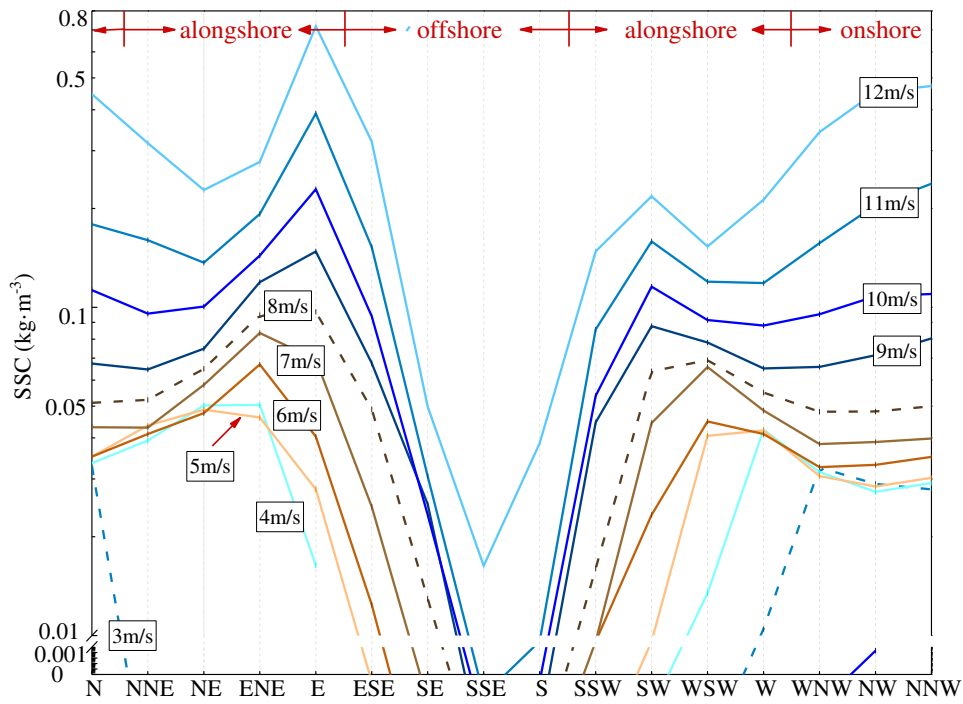
described in Fig. 5. Overall, the sediment concentration varied with large amplitude by different wind

398 events, and the incipient speed for sediment motion was disparate among wind directions. Onshore
399 winds (NW, N, NNW, WNW) were more subjected to enhanced local SSC, and speeds above 2 m/s
400 were sufficient to evoke sediment behavior. Comparably, offshore winds (SE, S, SSE, ESE) were
401 weak in increasing the SSC of the site, and slight ascent could be observed only when the wind speed
402 exceeded 5 m/s. For alongshore winds, sediment was activated when the speed was greater than 4
403 m/s.

404 The processes of sediment dynamics of the water intake can be approximately illustrated by 3
405 stages based on 2 wind speed thresholds: (1) within the speed range of 0~3 m/s, less sediment was
406 activated or transported into the observed site, indicating a relatively calm circumstance of the entire
407 lake, and onshore winds played a controlling role in SSC rising, while alongshore winds began to
408 take effect later this stage; (2) as the speed increased and was below 8 m/s, the sediment bed was
409 triggered and the SSC in the study site gradually increased (0.02~0.1 kg/m³) along with wind speed,
410 and alongshore winds acted more powerfully than onshore winds in this stage; (3) a prodigious
411 increase in SSC occurred (0.1~0.8kg/m³) once the wind speed was above 8 m/s, a large amount of
412 sediment was suspended, and complex migration occurred due to the dramatic hydrodynamic
413 behavior as well.

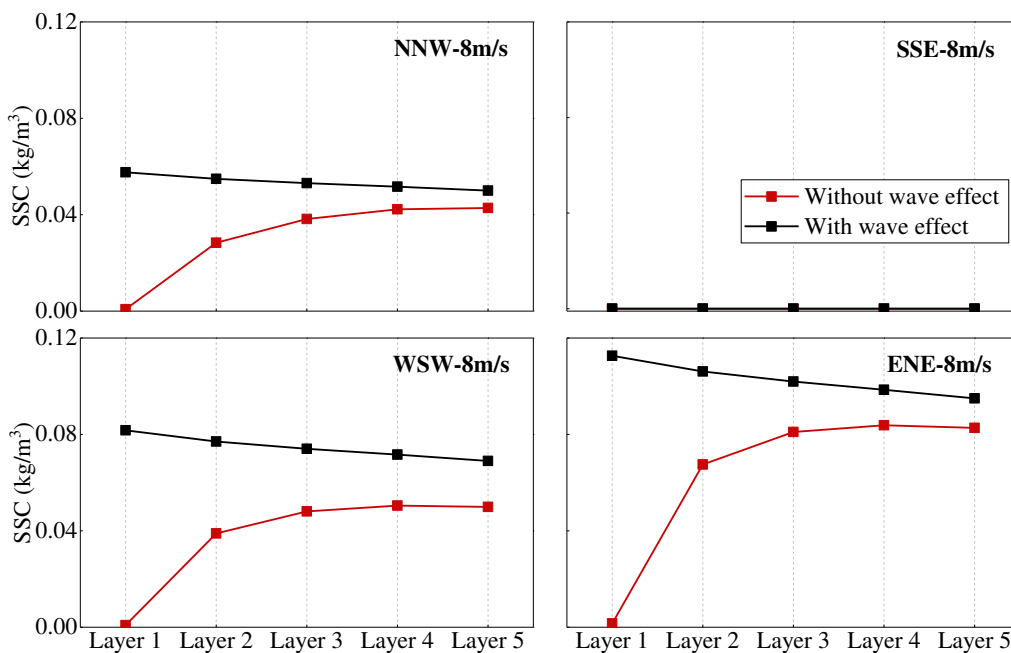
414 To observe the contribution of migration to SSC at the water intake area, the local wave effect
415 was removed by revising the significant wave height of this grid as 0 m. The modified wave field was
416 then used in the MT model to compare the change in local SSC. [Figure.6](#) shows the comparison of 4
417 typical wind conditions: layers 1 to 5 represent the bottom of the water column to the top. The
418 sediment of the bottom layer was unable to be suspended when the effect of local wave-induced shear

419 stress was excluded, and the SSC of the second layer decreased by 35% ~ 50%. However, the
 420 concentration of the surface layer was only reduced by 12% ~ 27%. The slight change in SSC in the
 421 overlying water manifested the leading role of migration to local sediment aggregation while the
 422 effect of resuspension was comparatively poor.



423

424 **Fig. 5** Simulated SSC of the water intake area under different model conditions



425

426

Fig. 6 Stratified SSC of the water intake area under different local wave conditions

427

4.2 The prediction of turbidity based on the simulation model

428

429

430

The simulated SSC values in the water intake area were matched to the measured turbidity to observe the relationship between the two series. The values were calculated according to the recorded wind conditions with linear interpolation between adjacent working conditions.

431

432

433

434

435

436

437

438

The pattern model representation (PMR) was then introduced to measure the trend similarity of the time series (Wang et al. 2004): it is based on piecewise linear representation and overcomes the problem of time series mismatch based on point distance. According to the number of segmentations, the series pattern distance (SPD) calculated by different scale features reflects the different similarities of series, and a pattern represents one segment monotone's tendency. In this paper, the pattern was defined as triple, that was {up, hold, down}, and was represented as $P = \{1,0,-1\}$ correspondingly to facilitate calculation. Let $L = (l_1, l_2, \dots, l_i)$ be a time series. The element of the pattern set $p \in P$ was marked by introducing the amplitude threshold σ :

$$p = \begin{cases} 1 & \text{when } (l_i - l_{i-1})/l_{i-1} < -\sigma \\ 0 & \text{when } |(l_i - l_{i-1})/l_{i-1}| \leq \sigma \\ -1 & \text{when } (l_i - l_{i-1})/l_{i-1} > \sigma \end{cases} \quad (26)$$

439

440

The time series of S_c and T were finally transformed into order sets of the (pattern value, timestamp) pair:

$$S'_c = [(p_{S_c}(1), t_1), \dots, (p_{S_c}(n), t_n)] \quad (27)$$

$$T' = [(p_T(1), t_1), \dots, (p_T(n), t_n)] \quad (28)$$

441

442

Where S'_c and T' were the pattern series of S_c and T ; t_i was the time phase; $p_{S_c}(i)$ and $p_T(i)$ were the pattern elements of the two series keeping from t_{i-1} to t_i . The mean pattern distance (D)

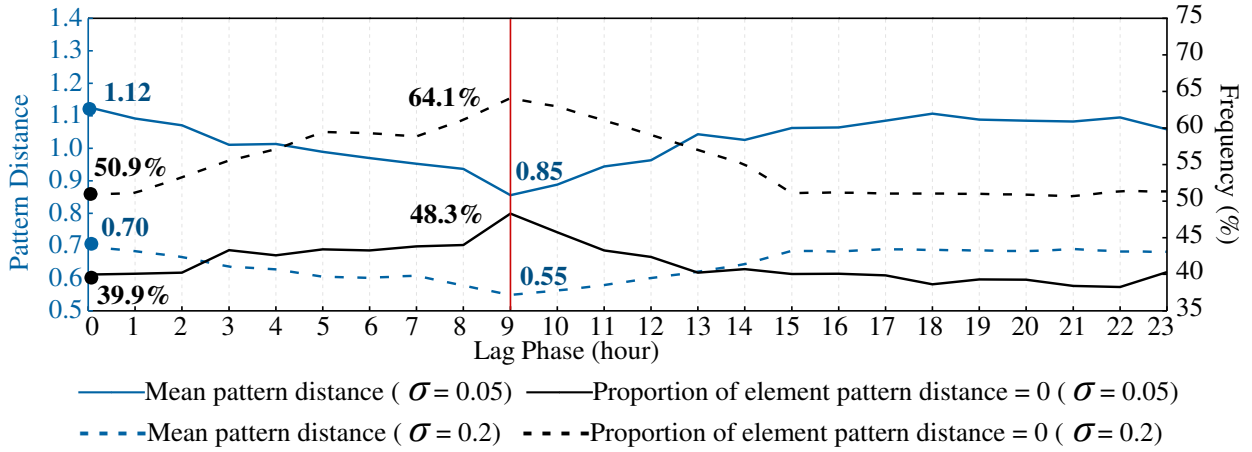
443 was calculated as Eq. 29:

$$D = \frac{1}{N} (p_{Sc}(i) - p_T(i))^2 \quad (29)$$

444 Where N is the number of pattern segments; $(p_{Sc}(i) - p_T(i))^2$ is the element pattern distance.

445 Considering that the error of turbidity prediction varied from 5% to above 50 %, 20% was a
446 relatively low error according to existing studies (Kennedy et al. 2015; Zhang et al. 2004), the
447 variation amplitude threshold σ for pattern model representation was selected as 0.05 and 0.2 in this
448 study. The quantified similarity of the hourly trends of the calculated SSC and turbidity (Fig.7)
449 showed that the two temporal sets were synchronous for approximately 40% of all conditions and
450 obtained a mean pattern distance of 1.12 according to Eq. 30 when σ was 0.05, for $\sigma = 0.2$; the
451 frequency of element pattern distance = 0 and D was 50.9% and 0.70, respectively. Because SSC
452 was a short-term response parameter, which replied slowly to the wind condition rather than being
453 completely synchronized, its temporal trend and turbidity were less synchronous as well due to the
454 lag reaction of sediment resuspension and transportation, and the lag time frame also reflected the
455 water-column residence time of sediments resuspended by wind-generated wave activity. The pattern
456 distance of 0 to 23 lag hours was considered in this paper to find the optimum lag frame of the study
457 area (Fig. 7), and the state of the 9-hour lag obtained the best performance for all conditions. Owing
458 to the 2-h delay to pump raw water from the intake area to the waterworks, a 7-h lag was believed to
459 be the optimal state for the current study. The obtained results conformed to the existing research
460 results (Zhao et al., 2018) that the lag phase varied from 2 to 10 depending on local conditions. The
461 shortest D and the highest proportion of synchronous cases decreased to 0.85 and increased to 48.2%
462 at $\sigma = 0.05$, 0.55 and 64.1% for $\sigma = 0.2$, respectively. For the series of turbidity and 7-hour-lag

463 wind speeds, the values were 48.9% and 1.04 at $\sigma = 0.2$, which manifested the progress of the
 464 current model.



465

466

Fig. 7 The comparison of pattern distance under different σ and lag phase

467

468

469

470

471

The S_c calculated according to Eq. 26 and the turbidity series were all managed as day-mean series to weaken the interference of extreme values. The consistency checking was adopted then through intraclass correlation coefficient (ICC), which ranges from 0 to 1. It shows a weak consistency when the coefficient is below 0.4, and a strong consistency as the value exceeds 0.7. The formula of ICC is:

$$ICC = \frac{\sum_i^n (X_{1i} - \bar{X})(X_{2i} - \bar{X})}{(n - 1)s_x^2} \quad (30)$$

472

473

Where, $X_1(X_{11}, X_{12}, \dots, X_{1i})$ and $X_2(X_{21}, X_{22}, \dots, X_{2i})$ are the variable sequences; \bar{X} is the joint mean; s_x is the combined variance.

474

475

476

477

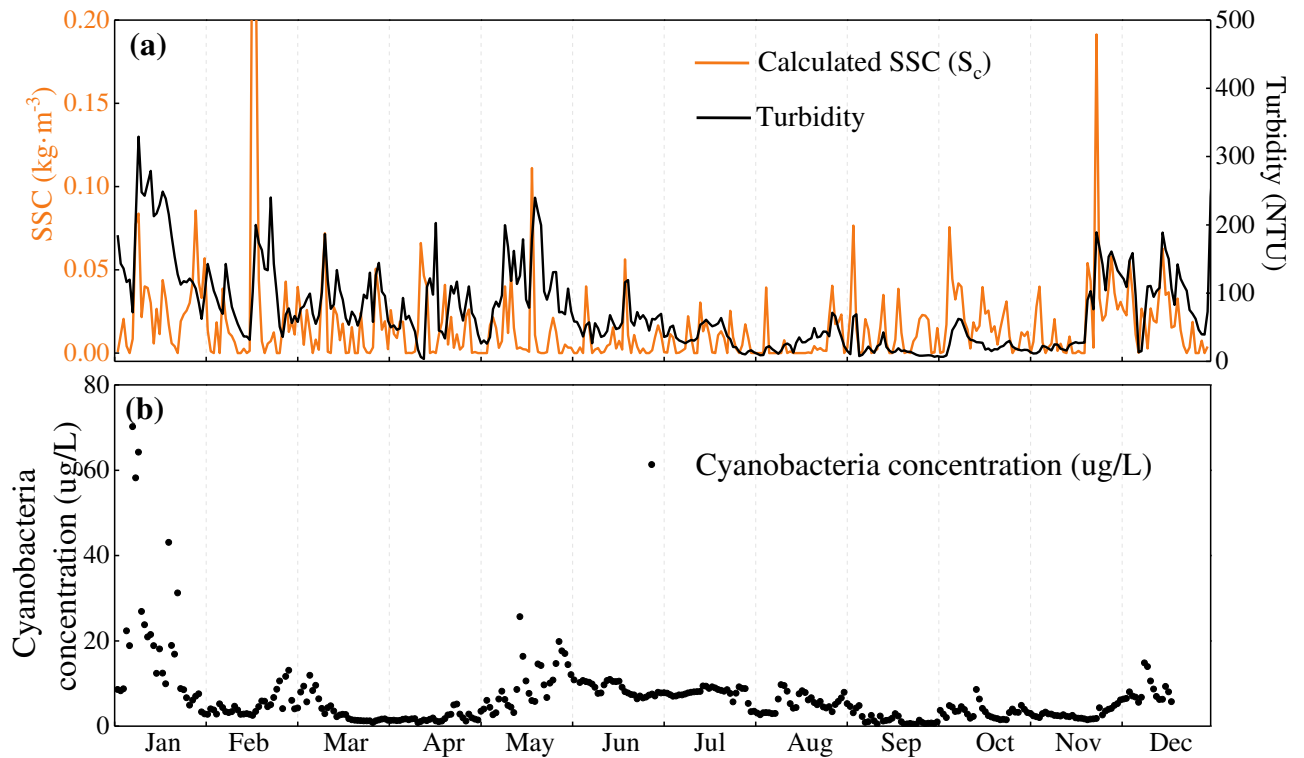
478

The coefficient achieved 0.56 between the predicted and measured series. A strong trend correlation was confirmed among the two series, but errors were always existed in variation amplitude. In addition, the sequences seemed to coincide with each other more satisfactorily (Fig. 8 a) at peak values. Because higher values were all more subjected to occurred during winter, which was characterized by typical onshore (northwesterly) winds with high speed. This could be used to further

479 confirm that the strong wind force of northwestern winds and the induced waves and currents readily
480 loosened the sediment structure and stimulated particles to resuspend and migrate for the long fetch
481 and consequently considerable energy, thus effectively developing a turbidity maximum at the water
482 intake.

483 The high similarity of modeling SSC and measured turbidity confirmed the reasonability of the
484 simulation results and showed that the turbidity of the study area was strongly related to sediment
485 particles. However, it should also be noticed that distinguished discrepancies were presented during
486 January and from September to November. For the former, the turbidity was distinctly the largest
487 among the whole year but the value of SSC remained approximate to other months, while the two
488 items shared extremely similar tendencies. The relatively high concentration of cyanobacteria (Fig. 8
489 b) may have engendered this deviation since the aggregation of the alga increased the background
490 turbidity, which was insensitive to the wind conditions. Similar phenomena can be observed in May
491 and December as well with comparatively inconspicuous states. For the period of September to
492 October, the SSC fluctuated remarkably, while the turbidity remained relatively low and steady, which
493 may be attributed to the wind conditions characterized by multiple prevailing directions (Fig. 2).
494 Because the process of wind energy transfer was time-consuming, only winds in a specific situation
495 acted continuously on the water surface and enabled significant wave heights, thus increasing friction
496 drag between air and the water surface and ultimately activating sediment motion. The simulated SSC
497 used in the analysis was conducted from models reaching stability, however, the polytropic winds
498 failed to achieve it in actual circumstances that caused the deviation. And the ICC reached 0.63 for
499 the time without high cyanobacteria concentration and volatile wind condition (Feb. ~ Apr.、 Jun. ~

500 Aug., Nov. ~ Dec.).



501

502

Fig. 8 Day-mean series of: (a) S_c and turbidity; (b) Cyanobacteria concentration

503

504

505

506

507

The obtained results showed that the model was prospective for predicting the tendency of raw water turbidity according to weather forecasts. For the precise prediction of hourly weather conditions that have achieved an advance of 1-3 days, the current model is supposed to foresee the general variation in turbidity over the same time span. The reserved time was crucial for waterworks to adjust the operation parameter, correspondingly improving the efficiency for management.

508

5 Conclusions

509

510

511

The current study investigated the effect of wind forces on the hydrodynamic and sediment distribution of Lake Taihu based on field simulation and further observed the genesis of suspended sediment at the water intake area under typical wind conditions. Main conclusions can be drawn

512 follows:

513 (1) Areas exposed to long wind fetches were more subjected to activated hydrodynamic behavior,
514 leading to intensive resuspension. By the effect of typical onshore (NNW) winds, sediment
515 transported from the central region and suspended at the local area together contributed to the high
516 SSC at the water intake, whereas East Taihu Bay and the littoral zone were the main suppliers for the
517 case of alongshore (WSW and ENE) winds. Offshore (SSE) winds could hardly promote sediment
518 motion at the leeward bank, thus resulting in extremely low SSC at the site.

519 (2) Seven-hour was considered to be the optimum lag frame in this paper. The intraclass
520 correlation coefficient of the modeled SSC and measured turbidity with an 7-h lag achieved 0.56 in
521 general, and reached 0.63 when discarded months with high cyanobacteria concentration and volatile
522 wind. The high similarity of the two temporal series proved the feasibility and effectiveness of the
523 simulation model in turbidity prediction.

524 (3)The study applied field simulation to a site investigation that enabled a more comprehensive
525 acknowledgment of sediment behavior at the observation site by considering the redistribution of
526 particles in space and the lag reaction of wind force in time. In addition, this work provided an idea
527 for turbidity prediction of waterworks sharing similar environmental conditions (i.e., the water source
528 area is sensitive to wind changes, and the turbidity is mainly caused by sediment behaviors).

529 However, the model was only an approximate representation of the actual turbidity, and further
530 study of the quantitative relationship between simulated SSC and measured turbidity is required to
531 achieve a more definitive forecast. Attention should also be paid to the measurements of reducing the
532 turbidity in the water intake area based on the current work.

533

534 **Acknowledgements**

535 This work was supported by National Natural Science Foundation of China (51878597) and the
536 National Science and Technology Major Projects for Water Pollution Control and Treatment (No.
537 2017ZX07201003).

538 **Reference**

- 539 Aani SA, Bonny T, Hasan SW, Hilal N (2019) Can machine language and artificial intelligence
540 revolutionize process automation for water treatment and desalination ? Desalination 458: 84-
541 96. <https://dx.doi.org/10.1016/j.desal.2019.02.005>
- 542 Bohling B (2009) Measurements of threshold values for incipient motion of sediment particles with
543 two different erosion devices. J Marine Syst 75: 330 - 335.
544 <https://doi.org/10.1016/j.jmarsys.2007.01.014>
- 545 Burchard-Levine A, Liu SM, Vince F, Li MM, Ostfeld A, (2014) A hybrid evolutionary data driven
546 model for river water quality early warning. J Environ Manage 143: 8–16.
547 <https://dx.doi.org/10.1016/j.jenvman.2014.04.017>
- 548 Brand A, Lacy JR, Hsu K, et al (2010) Ind-enhanced resuspension in the shallow waters of South San
549 Francisco Bay: Mechanisms and potential implications for cohesive sediment transport. J Geo
550 Res Oceans 115: C11024. <https://10.1029/2010JC006172>
- 551 Brun-Cottan JC, (1976) Stokes settling and dissolution rate model for marine particles as a function
552 of size distribution. J Geophys Res 81: 1601 - 1606. <https://10.1029/JC081i009p01601>
- 553 Chao X, Jia Y, Shields FD, Wang S, Cooper CM (2008) Three-dimensional numerical modeling of
554 cohesive sediment transport and wind wave impact in a shallow oxbow lake. Adv Water Resour
555 31: 1004 - 1014. <https://dx.doi.org/10.1016/j.advwatres.2008.04.005>
- 556 Hasselmann K, Barnett TP, Bouws E, et al (1973) Measurements of wind-wave growth and swell
557 decay during the Joint North Sea Wave Project (JONSWAP). Dtsch Hydrogr Z 8: 1 - 95.
558 <https://doi.org/10.1093/ije/27.2.335>

559 Hou J, Wang C, Wang PF, Qian J (2013) Temporal variability and spatial distribution of granulometric
560 composition of surface sediments and classification in Taihu Lake. *J Hohai Univ (Nat Sci)* 41:
561 114 – 119. <https://doi.org/10.3876/j.issn.1000-1980.2013.02.004> . (in Chinese)

562 Hu CH, Hu WP, Zhang FB, et al (2006) Sediment resuspension in the Lake Taihu, China. *Chinese Sci*
563 *Bull* 51:731 – 737. <https://doi.org/10.1007/s11434-006-0731-2>

564 Huang SB, Li KM, Jiang GQ, et al (2013) Research on Water Exchange in Pearl River Estuary based
565 on MIKE3 Model. *Environ Sci Manage* 38:134 – 140.

566 Jalil A, Li YP, Zhang K, et al (2019) Wind-induced hydrodynamic changes impact on sediment
567 resuspension for large, shallow Lake Taihu, China. *Int J Sediment Res* 34: 18 – 28.
568 <https://doi.org/10.1016/j.ijsrc.2018.11.003>

569 Jin KR, Ji ZJ (2001) Calibration and verification of a spectral wind–wave model for Lake Okeechobee.
570 *Ocean Eng* 28: 571 – 584. [https://doi.org/10.1016/S0029-8018\(00\)00009-3](https://doi.org/10.1016/S0029-8018(00)00009-3)

571 Kennedy MJ, Gandomi AH, Miller CM, (2015) Coagulation modeling using artificial neural networks
572 to predict both turbidity and DOM-PARAFAC component removal. *J Environ Chem Eng* 3:
573 2829 – 2838. <http://dx.doi.org/10.1016/j.jece.2015.10.010>

574 Kessarkar PM, Rao VP, Shynu R, et al (2009) Wind-driven estuarine turbidity maxima in Mandovi
575 Estuary, central west coast of India. *J Earth Sys Sci* 118: 369 – 377.
576 <https://dx.doi.org/10.1007/s12040-009-0026-5>

577 Komen GJ, Cavaleri L, Donelan M, et al (1994) Dynamics and Modelling of Ocean Waves. *Dynam*
578 *Atmos Oceans* 25: 276-278. [https://doi.org/10.1016/0377-0265\(95\)00469-6](https://doi.org/10.1016/0377-0265(95)00469-6)

579 Kuang C, Wang YB, Gu J, Lei G (2016) Study of hydrodynamics using a bi-directional wave-current

580 coupled model in Haitan Bay, Fujian province. J Tongji Univ (Nat Sci) 8: 1212 - 1220.
581 <https://doi.org/10.11908/j.issn.0253-374x.2016.08.011>. (in Chinese)

582 Kumagai M (1988) Predictive model for resuspension and deposition of bottom sediment in a lake.
583 Jpn J Limnol 49: 185 - 200. <https://doi.org/10.3739/rikusui.49.185>

584 Li YP, Tang CY, Wang JW, et al (2016) Effect of wave-current interactions on sediment resuspension
585 in large shallow Lake Taihu, China. Environ Sci Pollut Res 24: 4029 - 4039.
586 <https://doi.org/10.1007/s11356-016-8165-0>

587 Luo LC, Qin BQ, Zhu GW (2004) Sediment distribution and the maximum resuspension depth with
588 disturbance in Lake Taihu[J]. J Sed Res 1: 9 - 14. [https://doi.org/CNKI:SUN:NSYJ.0.2004-01-](https://doi.org/CNKI:SUN:NSYJ.0.2004-01-001)
589 [001](https://doi.org/CNKI:SUN:NSYJ.0.2004-01-001) . (in Chinese)

590 Luo LC, Qin BQ (2003) Numerical simulation based on a three-dimensional shallow-water
591 hydrodynamic model in Lake Taihu -Current circulations in Lake Taihu with prevailing wind-
592 forcing[J]. J Hydrodyn 18() 686 - 691. (in Chinese)

593 Luettich RA, Harleman DR, Somlyódy L (1990) Dynamic behavior of suspended sediment
594 concentrations in a shallow lake perturbed by episodic wind events. Limnol Oceanogr 35:
595 1050 - 1067. <https://doi.org/10.4319/lo.1990.35.5.1050>

596 Pang Y, Li YP, Luo LC (2006) Study on the simulation of transparency of Lake Taihu under different
597 hydrodynamic conditions. Sci China: Ser D 49: 162 - 175. [https://doi.org/10.1007/s11430-006-](https://doi.org/10.1007/s11430-006-8116-6)
598 [8116-6](https://doi.org/10.1007/s11430-006-8116-6)

599 Parchure T, Mehta A (1985) Erosion of Soft Cohesive Sediment Deposits. J Hydraul Eng 111: 1308-
600 1326. [https://doi.org/10.1061/\(ASCE\)0733-9429\(1985\)111:10\(1308\)](https://doi.org/10.1061/(ASCE)0733-9429(1985)111:10(1308))

601 Partheniades E (1965) Erosion and Deposition of Cohesive Soils. Am Soc Civ Eng 91: 190-192.
602 <https://doi.org/10.3109/15622970109026808>

603 Qin BQ, Hu WP, Gao G, Luo LC, Zhang JS (2004) Dynamics of sediment resuspension and the
604 conceptual schema of nutrient release in the large shallow Lake Taihu, China. Chinese Sci Bull
605 49: 54 - 64. <https://doi.org/10.1007/BF02901743>

606 Qin B, et al (2005) Models and estimation methods of endogenous nutrient release from sediments
607 of large shallow lakes: A case study of Taihu Lake. Sci China Ser D 49: 38-50.
608 <https://dx.doi.org/10.3969/j.issn.1674-7240.2005.z2.004> . (in Chinese)

609 Qin BQ, Xu PZ, Wu QL et al (2007) Environmental issues of Lake Taihu, China. Hydrobiologia 581:
610 3 - 14. <https://doi.org/10.1007/s10750-006-0521-5>

611 Qiu H, Zhao QH, Zhu WJ (2013) Model simulation of suspended solids in taihu lake under real
612 meteorological condition. Oceanologia et Limnologia Sinica 44: 1418 - 1426.
613 <https://dx.doi.org/CNKI:SUN:HYFZ.0.2013-06-002> . (in Chinese)

614 Sheng Y, Lick W, (1979) The transport and resuspension of sediments in a shallow lake. J Geophys
615 Res 84: 1809 - 1826. <https://dx.doi.org/10.1029/JC084iC04p01809>

616 Shu YH, Gao CC, (2021) Numerical simulation of wind-driven current and pollutant transport and
617 diffusion in Taihu Lake. Water Resour Prot 37: 121 - 127.
618 <https://dx.doi.org/10.3880/j.issn.1004-6933.2021.02.019> . (in Chinese)

619 Signell RP, Beardsley RC, Graber HC, et al. (1990) Effect of wave-current interaction on wind-driven
620 circulation in narrow, shallow embayments. J Geo Res Oceans 95: C6.
621 <https://10.1029/JC095iC06p09671>

- 622 Stone R (2011) China aims to turn tide against toxic lake pollution. *Sci* (New York, N.Y.) 333: 1210 –
623 1211. <https://dx.doi.org/10.1126/science.333.6047.1210>
- 624 Tang CY, Li YP, Acharya K, et al (2019) Impact of intermittent turbulent bursts on sediment
625 resuspension and internal nutrient release in Lake Taihu, China. *Environ Sci Pollut Res* 26:
626 16519 – 16528. <https://dx.doi.org/10.1007/s11356-019-04847-2>
- 627 Tang CY, Li YP, He C, Acharya K (2020) Dynamic behavior of sediment resuspension and nutrients
628 release in the shallow and wind-exposed Meiliang Bay of Lake Taihu. *Sci Total Environ* 708:
629 135131. <https://dx.doi.org/10.1016/j.scitotenv.2019.135131>
- 630 Tang LL, Wang P, Yao Q (2011) Three-dimensional numerical simulation of current, waves and
631 sediment transport in Taihu Lake. *Water Resour Prot* 27: 1 – 5.
632 <https://dx.doi.org/10.3969/j.issn.1004-6933.2011.02.001> . (in Chinese)
- 633 Wang D, Rong G (2004) Pattern distance of time series. *J Zhejiang Univ (Eng Sci)* 29: 53 – 61.
634 <https://dx.doi.org/10.1007/BF02873091>
- 635 Wang JD, Qi WG (2009) Prediction of River Water Turbidity Based on EMD-SVM. *Acta Electronica*
636 *Sinica* 37: 2130 – 2133. <https://dx.doi.org/10.1016/j.apm.2007.10.019> . (in Chinese)
- 637 Wu TF, Qin BQ, Zhu GW et al (2013) Modeling of turbidity dynamics caused by wind-induced waves
638 and current in the Taihu Lake. *Int. J Sed Res* 28: 139 – 148. [https://dx.doi.org/10.1016/S1001-
639 6279\(13\)60026-8](https://dx.doi.org/10.1016/S1001-6279(13)60026-8)
- 640 Wu TF, Qin BQ, Brookes D, et al (2018) Spatial distribution of sediment nitrogen and phosphorus in
641 Lake Taihu from a hydrodynamics-induced transport perspective. *Sci Total Environ* 650: 1554 –
642 1565. <https://dx.doi.org/10.1016/j.scitotenv.2018.09.145>

643 Xu RC, Pang Y, Hu ZB, Zhu TY (2020) Relationship between water age and hydraulic residence time
644 in Taihu Lake and parameter sensitivity. *Water Resour Prot* 36: 38 - 43.
645 <http://dx.doi.org/10.3880/j/issn.1004-6933.2020.03.007> . (in Chinese)

646 Yue SL (1995) Turbidity of water. *China Water & Wastewater* 4: 33 - 35. (in Chinese)

647 Zhao JJ, Wei ZP, Liu J, (2018) Numerical simulation of hydrodynamic force to suspended sediment
648 of Taihu Lake. *Port Waterway Eng* 550: 119 - 125. <https://dx.doi.org/10.16233/j.cnki.issn1002-4972.20181205.008> . (in Chinese)

650 Zhang P, Chen XL, Lu JZ, Zhang W (2015) Assimilation of remote sensing observations into a
651 sediment transport model of China's largest freshwater lake: spatial and temporal effects.
652 *Environ Sci Pollut Res* <https://dx.doi.org/10.1007/s11356-015-4958-9>

653 Zhao QH, Chen SQ, Chen SY (2018) Turbidity in response to wind speed, wind direction and wind
654 duration in Gonghu Bay, Lake Taihu. *J Lake Sci* 30: 1587 - 1598.
655 <https://dx.doi.org/10.18307/2018.0610> . (in Chinese)

656 Zhang YL, Qin BQ, Chen WM, et al (2004) A study on total suspended matter in lake Taihu. *Res*
657 *Environ Yangtze Basin* 13; 266 - 271. <https://10.3969/j.issn.1004-8227.2004.03.014>

658 Zhang YP, Yao XY, Wu Q, et al (2021) Turbidity prediction of lake-type raw water using random
659 forest model based on meteorological data: A case study of Tai lake, China. *J Environ Manage*
660 290:112657. <https://doi.org/10.1016/j.jenvman.2021.112657>

661 Zheng SS, Wang PF, Wang C, Hou J (2015) Sediment resuspension under action of wind in Taihu
662 Lake, China. *Int J Sed Res* 30: 48 - 62. [https://dx.doi.org/10.1016/S1001-6279\(15\)60005-1](https://dx.doi.org/10.1016/S1001-6279(15)60005-1)

663 **Statements and Declarations**

664 **Funding:** This work was supported by National Natural Science Foundation of China (51878597)
665 and the National Science and Technology Major Projects for Water Pollution Control and Treatment
666 (No. 2017ZX07201003).

667 **Author Contributions:** Xinyu Yao: Methodology, Validation, Formal analysis, Writing - Original
668 Draft; Xiaowei Liu: Project administration, Writing - Review & Editing; Yongchao Zhou: Project
669 administration, Writing - Review & Editing; Liang Zhang: Resources, Data Curation; Zhixu Zhou:
670 Resources, Data Curation; Yiping Zhang: Conceptualization, Writing - Review & Editing,
671 Supervision.

672 **Ethics approval:** All the sources have been cited appropriately and there is no such issue during this
673 study.

674 **Consent to participate:** All the authors will participate in review and publication process.

675 **Consent to publish:** All the authors have given their consent to publish this study.

676 **Competing Interests:** The authors have no relevant financial or non-financial interests to disclose.

677 **Availability of Data and Materials:** Not applicable.

678

679

Supplementary Files

This is a list of supplementary files associated with this preprint. Click to download.

- [SupplementaryInformation.pdf](#)